



Publication Year	2016
Acceptance in OA @INAF	2020-05-14T14:24:23Z
Title	The Swift-BAT monitoring reveals a long-term decay of the cyclotron line energy in Vela X-1
Authors	LA PAROLA, VALENTINA; CUSUMANO, GIANCARLO; SEGRETO, ALBERTO; D'AI', ANTONINO
DOI	10.1093/mnras/stw1915
Handle	http://hdl.handle.net/20.500.12386/24821
Journal	MONTHLY NOTICES OF THE ROYAL ASTRONOMICAL SOCIETY
Number	463

The *Swift*-BAT monitoring reveals a long-term decay of the cyclotron line energy in Vela X-1

V. La Parola,[★] G. Cusumano, A. Segreto and A. D’Aì

INAF, Istituto di Astrofisica Spaziale e Fisica Cosmica, Via U. La Malfa 153, I-90146 Palermo, Italy

Accepted 2016 July 29. Received 2016 July 29; in original form 2016 May 23

ABSTRACT

We study the behaviour of the cyclotron resonant scattering feature (CRSF) of the high-mass X-ray binary Vela X-1 using the long-term hard X-ray monitoring performed by the Burst Alert Telescope (BAT) on board *Swift*. High-statistics, intensity-selected spectra were built along 11 years of BAT survey. While the fundamental line is not revealed, the second harmonic of the CRSF can be clearly detected in all the spectra, at an energy varying between ~ 53 and ~ 58 keV, directly correlated with the luminosity. We have further investigated the evolution of the CRSF in time, by studying the intensity-selected spectra built along four 33-month time intervals along the survey. For the first time, we find in this source a secular variation in the CRSF energy: independent of the source luminosity, the CRSF second harmonic energy decreases by ~ 0.36 keV yr⁻¹ between the first and the third time intervals, corresponding to an apparent decay of the magnetic field of $\sim 3 \times 10^{10}$ G yr⁻¹. The intensity-cyclotron energy pattern is consistent between the third and the last time intervals. A possible interpretation for this decay could be the settling of an accreted mound that produces either a distortion of the poloidal magnetic field on the polar cap or a geometrical displacement of the line forming region. This hypothesis seems supported by the correspondence between the rate of the line shift per unit accreted mass and the mass accreted on the polar cap per unit area in Vela X-1 and Her X-1, respectively.

Key words: stars: magnetic field – pulsars: individual: Vela X-1 – X-rays: binaries.

1 INTRODUCTION

Vela X-1 is a wind-accreting neutron star (NS) with a spin period of ~ 283 s (McClintock et al. 1976), rotating in an 8.9 d (van Kerkwijk et al. 1995) orbit around the B0.5Ib supergiant HD 77523 (Hiltner, Werner & Osmer 1972), at a distance 1.9 ± 0.2 kpc (Sadakane et al. 1985). The mean luminosity of the source is 5×10^{36} erg s⁻¹ (Fürst et al. 2010), and the flux shows a great variability even at short time-scales (hours), with the source going from off-states to giant flares up to a few Crab (Kreykenbohm et al. 2008).

NSs in high-mass X-ray binaries (HMXBs) are characterized by intense magnetic fields ($\sim 10^{12}$ G) that in several sources can be directly measured through the energy of characteristic absorption lines called cyclotron resonant scattering features (CRSF). A strong magnetic field causes the motion of the electrons perpendicular to the magnetic field in the accreting plasma to be quantized in discrete Landau levels, and photons with energies corresponding to these levels undergo resonant scattering producing an absorption feature in their spectra.

In Vela X-1, an absorption line feature at 55 keV was first reported by Kendziorra et al. (1992) with data from the High Energy X-ray Experiment (HEXE), while Makishima & Mihara (1992) and Choi et al. (1996) reported an absorption feature at lower energy (~ 30 keV) from *Ginga* data. Later observations failed to detect this low-energy feature, revealing only one absorption line at 53 \sim 55 keV (Orlandini et al. 1998; La Barbera et al. 2003; Kreykenbohm et al. 2008). Kretschmar et al. (1997) with HEXE, Kreykenbohm et al. (2002) with *RXTE*, Schanne et al. (2007) with *INTEGRAL*, and Maitra & Paul (2013) and Odaka et al. (2013) with *Suzaku* confirmed the presence of both features, with energies varying between ~ 23 and ~ 27 keV and between ~ 45 and ~ 54 keV, respectively. The low-energy feature, interpreted as the fundamental CRSF, is considerably weaker than its second harmonic. Fürst et al. (2014) analysed two *NuSTAR* observations with different luminosity levels detecting both features, but while the harmonic is always highly significant, the fundamental is barely detectable in the observation at higher intensity. They also show that the depths of the two lines are anti-correlated and they interpret this result as due to photon spawning (see e.g. Schönherr et al. 2007), suggesting this as the likely explanation of the elusiveness of the fundamental. Moreover, Fürst et al. (2014) report for the first time in this source a correlation

[★]E-mail: laparola@ifc.inaf.it

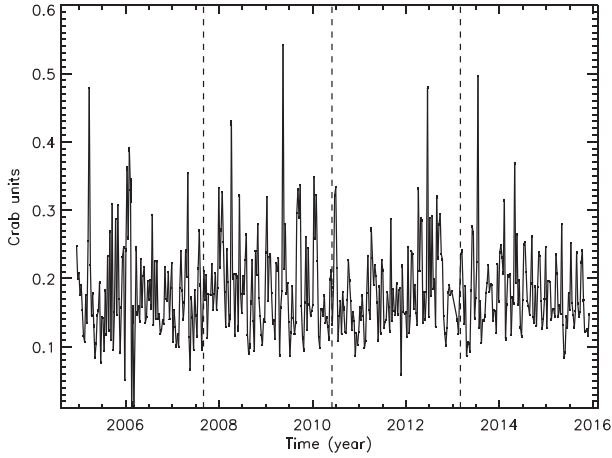


Figure 1. BAT 15–100 keV light curve of Vela X-1. The bin time is equal to the orbital period (8.964 d). The vertical dashed lines mark the four time-selected intervals used to probe the line energy versus luminosity relation.

between the harmonic line energy and the flux, as expected in the subcritical accretion regime (Becker et al. 2012).

In this paper, we performed a detailed spectral analysis of Vela X-1 based on the 11 year monitoring performed by the Burst Alert Telescope (BAT; Barthelmy et al. 2005) on board *Swift* (Gehrels et al. 2004). The large BAT field of view (1.4 sr half coded), together with the *Swift* observatory pointing strategy (several pointings per day towards different directions of the sky), allows BAT to have the source within its field of view nearly every day.

This paper is organized as follows. Section 2 describes the data reduction and the calibration procedures applied to the BAT data. In Section 3, we describe the spectral analysis and in Section 4 we discuss our results.

2 DATA REDUCTION

The BAT survey data collected between 2004 December and 2015 November were retrieved from the HEASARC public

Table 1. Spectral fit results from the count-rate-selected spectra extracted along the entire survey monitoring. E_H , σ_H and D_H are the energy, width and depth of the CRSF second harmonic, respectively. kT and τ are the plasma temperature and optical depth, respectively. The input photon temperature attains to the soft X-ray energy range and it is not well constrained by the BAT data. Therefore, it has been kept fixed to 0.82 keV for all the spectra, which is the average value obtained in a pre-analysis of the spectra. L_{36} is the luminosity of the continuum evaluated in the 1–150 keV energy range in units of 10^{36} erg s^{-1} . The quoted reduced χ^2 is evaluated for 32 degrees of freedom.

Sp	E_H (keV)	σ_H (keV)	D_H	kT (keV)	τ	L_{36} (erg s^{-1})	χ^2
1	$53.4^{+0.3}_{-0.3}$	$7.3^{+0.2}_{-0.2}$	$15.3^{+0.9}_{-0.9}$	$8.5^{+0.1}_{-0.1}$	$7.8^{+0.1}_{-0.1}$	1.73	1.27
2	$53.8^{+0.4}_{-0.4}$	$7.5^{+0.3}_{-0.3}$	$17.2^{+1.2}_{-1.2}$	$8.5^{+0.1}_{-0.1}$	$7.8^{+0.1}_{-0.1}$	2.74	1.10
3	$55.0^{+0.4}_{-0.4}$	$8.0^{+0.3}_{-0.3}$	$19.2^{+1.5}_{-1.4}$	$8.3^{+0.1}_{-0.1}$	$8.0^{+0.1}_{-0.1}$	3.06	1.26
4	$54.5^{+0.4}_{-0.3}$	$7.7^{+0.3}_{-0.3}$	$19.2^{+1.3}_{-1.2}$	$8.3^{+0.1}_{-0.1}$	$8.0^{+0.1}_{-0.1}$	3.40	1.44
5	$54.6^{+0.4}_{-0.4}$	$8.0^{+0.3}_{-0.3}$	$19.0^{+1.4}_{-1.3}$	$8.2^{+0.1}_{-0.1}$	$8.2^{+0.1}_{-0.1}$	3.74	1.12
6	$54.7^{+0.4}_{-0.4}$	$8.0^{+0.3}_{-0.3}$	$19.4^{+1.5}_{-1.4}$	$8.1^{+0.1}_{-0.1}$	$8.4^{+0.1}_{-0.1}$	4.02	1.15
7	$55.2^{+0.5}_{-0.4}$	$8.3^{+0.4}_{-0.4}$	$19.3^{+1.7}_{-1.6}$	$7.9^{+0.1}_{-0.1}$	$8.6^{+0.1}_{-0.1}$	4.27	0.78
8	$54.7^{+0.5}_{-0.4}$	$8.0^{+0.4}_{-0.4}$	$18.4^{+1.7}_{-1.5}$	$7.7^{+0.1}_{-0.1}$	$9.0^{+0.2}_{-0.2}$	4.45	0.99
9	$55.8^{+0.5}_{-0.5}$	$9.0^{+0.4}_{-0.4}$	24^{+2}_{-2}	$8.0^{+0.1}_{-0.1}$	$8.5^{+0.2}_{-0.2}$	5.03	0.70
10	$55.8^{+0.6}_{-0.6}$	$9.0^{+0.5}_{-0.5}$	21^{+2}_{-2}	$7.7^{+0.1}_{-0.1}$	$9.0^{+0.2}_{-0.2}$	5.10	1.24
11	$55.9^{+0.6}_{-0.6}$	$9.1^{+0.5}_{-0.4}$	23^{+3}_{-2}	$7.8^{+0.1}_{-0.1}$	$9.0^{+0.2}_{-0.2}$	5.60	1.04
12	$56.2^{+0.6}_{-0.6}$	$9.7^{+0.5}_{-0.5}$	26^{+2}_{-3}	$7.9^{+0.2}_{-0.2}$	$8.8^{+0.2}_{-0.2}$	6.00	1.15
13	$55.4^{+0.7}_{-0.6}$	$8.8^{+0.5}_{-0.5}$	22^{+3}_{-2}	$7.6^{+0.2}_{-0.1}$	$9.4^{+0.2}_{-0.2}$	6.04	1.33
14	$55.8^{+0.6}_{-0.6}$	$8.6^{+0.5}_{-0.5}$	19^{+2}_{-2}	$7.5^{+0.1}_{-0.1}$	$9.5^{+0.2}_{-0.2}$	6.23	1.38
15	$56.2^{+0.4}_{-0.8}$	$9.9^{+0.7}_{-0.7}$	26^{+2}_{-4}	$7.7^{+0.1}_{-0.2}$	$9.3^{+0.3}_{-0.2}$	6.71	1.36
16	$57.2^{+0.6}_{-0.5}$	$10.1^{+0.3}_{-0.3}$	$25.4^{+1.2}_{-1.1}$	$7.5^{+0.1}_{-0.1}$	$9.8^{+0.1}_{-0.1}$	6.79	1.34
17	$56.3^{+0.9}_{-0.8}$	$9.4^{+0.8}_{-0.7}$	21^{+4}_{-3}	$7.5^{+0.2}_{-0.2}$	$9.7^{+0.3}_{-0.3}$	7.15	1.04
18	$56.2^{+0.6}_{-0.6}$	$9.3^{+0.6}_{-0.5}$	24^{+3}_{-3}	$7.3^{+0.2}_{-0.1}$	$9.8^{+0.2}_{-0.2}$	7.63	1.77
19	$56.8^{+0.7}_{-0.7}$	$9.5^{+0.8}_{-0.5}$	24^{+4}_{-3}	$7.3^{+0.2}_{-0.1}$	$10.1^{+0.2}_{-0.4}$	8.12	0.80
20	$56.7^{+0.8}_{-0.9}$	$9.6^{+0.8}_{-0.7}$	22^{+2}_{-3}	$7.1^{+0.1}_{-0.1}$	$10.5^{+0.3}_{-0.3}$	8.67	1.09
21	$55.9^{+0.5}_{-0.5}$	$9.1^{+0.3}_{-0.3}$	$18.3^{+0.9}_{-0.9}$	$7.0^{+0.1}_{-0.1}$	$10.9^{+0.1}_{-0.1}$	8.92	1.92
22	$56.5^{+0.7}_{-0.9}$	$9.6^{+0.8}_{-0.7}$	23.0^{+2}_{-4}	$7.0^{+0.1}_{-0.2}$	$10.6^{+0.3}_{-0.3}$	9.84	1.48
23	$56.5^{+0.7}_{-0.6}$	$9.3^{+0.4}_{-0.3}$	$20.4^{+1.3}_{-1.2}$	$6.9^{+0.1}_{-0.1}$	$10.9^{+0.1}_{-0.1}$	10.10	1.26
24	$56.0^{+1.0}_{-0.8}$	$8.9^{+0.8}_{-0.7}$	19^{+4}_{-3}	$6.8^{+0.2}_{-0.1}$	$11.5^{+0.4}_{-0.4}$	10.31	1.37
25	$57.4^{+0.6}_{-0.6}$	$9.5^{+0.4}_{-0.4}$	$20.2^{+1.2}_{-1.1}$	$6.8^{+0.1}_{-0.1}$	$11.2^{+0.1}_{-0.1}$	10.76	1.47
26	$57.4^{+0.5}_{-1.0}$	$10.4^{+1.1}_{-0.8}$	22^{+1}_{-4}	$6.8^{+0.1}_{-0.2}$	$11.1^{+0.3}_{-0.1}$	13.21	1.01

archive¹ and processed with the `BAT_IMAGER` code (Segreto et al. 2010), a software built for the analysis of data from coded mask instruments that performs screening, mosaicking and source detection and produces scientific products of any revealed source.

Fig. 1 shows the light curve of Vela X-1 in the 15–100 keV band, with a bin time equal to the orbital period (8.964 d). The intensity of the source shows large fluctuations, up to one order of magnitude.

The spectral analysis is aimed to investigate the behaviour of the cyclotron features with luminosity. We produced background-subtracted spectra of the source at several count rate levels. The appropriate good time intervals for each count rate interval were selected based on the source 15–150 keV light curve with a bin time of 90 min, in the count rate range between 0.001 and 0.05 counts s⁻¹ pixel⁻¹, corresponding to an observed 15–150 keV luminosity range between 0.15 and 7.5×10^{36} erg s⁻¹. To define the boundaries of each count rate bin, we started from the lower count rate limit, and we increased the upper count rate limit with a step of 0.001 counts s⁻¹ pixel⁻¹ until a satisfactory signal-to-noise ratio of ~ 800 is reached, allowing for enough statistics for an adequate modelling of the second harmonic. Since a Crab spectrum with similar statistics shows the presence of systematic deviations with respect to a power law, we have applied to each Vela X-1 spectrum a systematic error to be added in quadrature to the statistical one. The systematic errors were derived fitting the Crab spectrum extracted from the entire survey monitoring with a power law and evaluating for each energy channel the values $|R_i - R_i^*|/R_i$, where R_i^* is the rate derived with the best-fitting power-law model in the i th channel and R_i is the Crab count rate in the same channel. We have verified that this correction (amounting to 2 per cent on average) is negligible with respect to the statistical errors for the channels above 40 keV. We used the official BAT spectral redistribution matrix.² We report errors on spectral parameters at the 68 per cent confidence level.

3 SPECTRAL ANALYSIS

To model the continuum emission of Vela X-1, we tested different spectral shapes. A simple power law modified with an exponential cut-off (`cutoffpl`) is not adequate to describe the data. Both an optically thick Comptonization (`comptt`) and a Fermi–Dirac cut-off provide an acceptable fit for the continuum emission, while the CRSF is well described with a Gaussian absorption profile (`gabs` in `XSPEC`). We verified that the choice between the two continuum models does not affect the best-fitting line parameters. The results presented in this paper refer to a continuum described with an optically thick Comptonization. The results of the spectral analysis are reported in Table 1. In all the spectra, we detect with high significance the second harmonic, while the fundamental cannot be detected in any of the spectra. Fig. 2 shows two representative spectra at different levels of intensity, and their residuals with respect to the relevant best-fitting model. Fig. 3 shows the best-fitting line parameters (energy, width, strength and equivalent width in panels A, B, C, D, respectively) as a function of the intrinsic source luminosity. The equivalent width was evaluated according to the definition

$$EW = \int 1 - \frac{F(E)}{F_C(E)} dE, \quad (1)$$

¹ <http://heasarc.gsfc.nasa.gov/docs/archive.html>

² <http://heasarc.gsfc.nasa.gov/docs/heasarc/caldb/data/swift/bat/index.html>

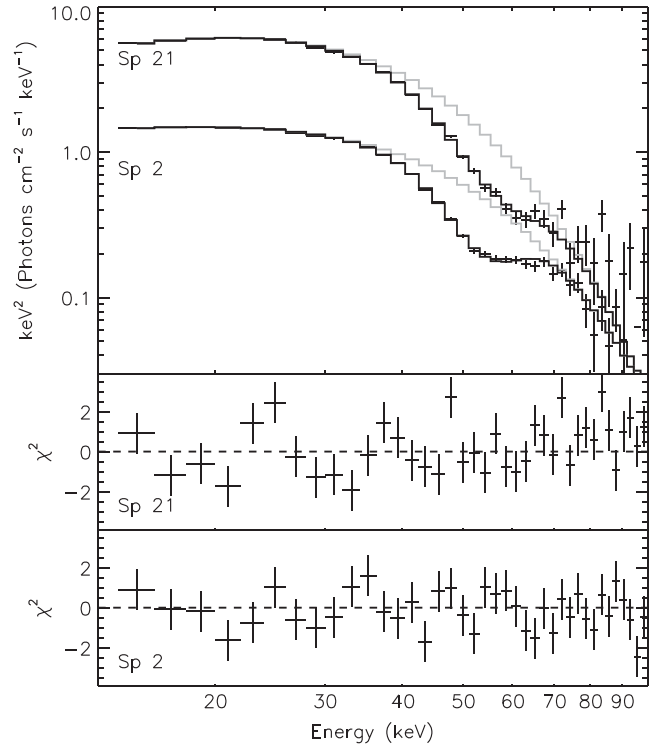


Figure 2. Data, best-fitting model and residuals for two representative spectra (spectra 2 and 21 in Table 1). In the top panel, the black line represents the best-fitting model (continuum and CRSF), while the grey line represents the best-fitting continuum model.

where F_C represents the intensity of the continuum and F is the intensity of the best-fitting model, evaluated in the 15–100 keV energy range. The line energy shows a clear direct correlation with the luminosity, ranging from ~ 53 keV at low luminosity to ~ 58 keV at high luminosity. The other line parameters also show a positive correlation with the luminosity. Panel E of Fig. 3 shows the Comptonization parameter, defined as $\gamma = \tau kT/m_e c^2$. We observe that γ is positively correlated with the luminosity, indicating a hardening of the continuum at higher luminosity, as already reported by Odaka et al. (2013) and Fürst et al. (2014) for Vela X-1 and by Klochov et al. (2011) for other accreting pulsars in subcritical accretion regime.

We have also investigated the long-term behaviour of this trend in time-selected intervals. To this aim, we have split the survey monitoring into four time intervals of the same length (33 months, see the dashed lines in Fig. 1), selecting the spectra in eight flux intervals for each of them. The results of the spectral analysis are plotted in Fig. 4 and listed in Table 2. We find that the line energy shows a systematic decrease between the first and the second time intervals and between the second and the third one, while there is no significant change between the third and the fourth intervals.

4 DISCUSSION AND CONCLUSIONS

We report on the analysis of the *Swift*-BAT spectral data of Vela X-1, focusing on the relation between the CRSF energy and luminosity in the overall timespan covered by BAT and in time-selected intervals.

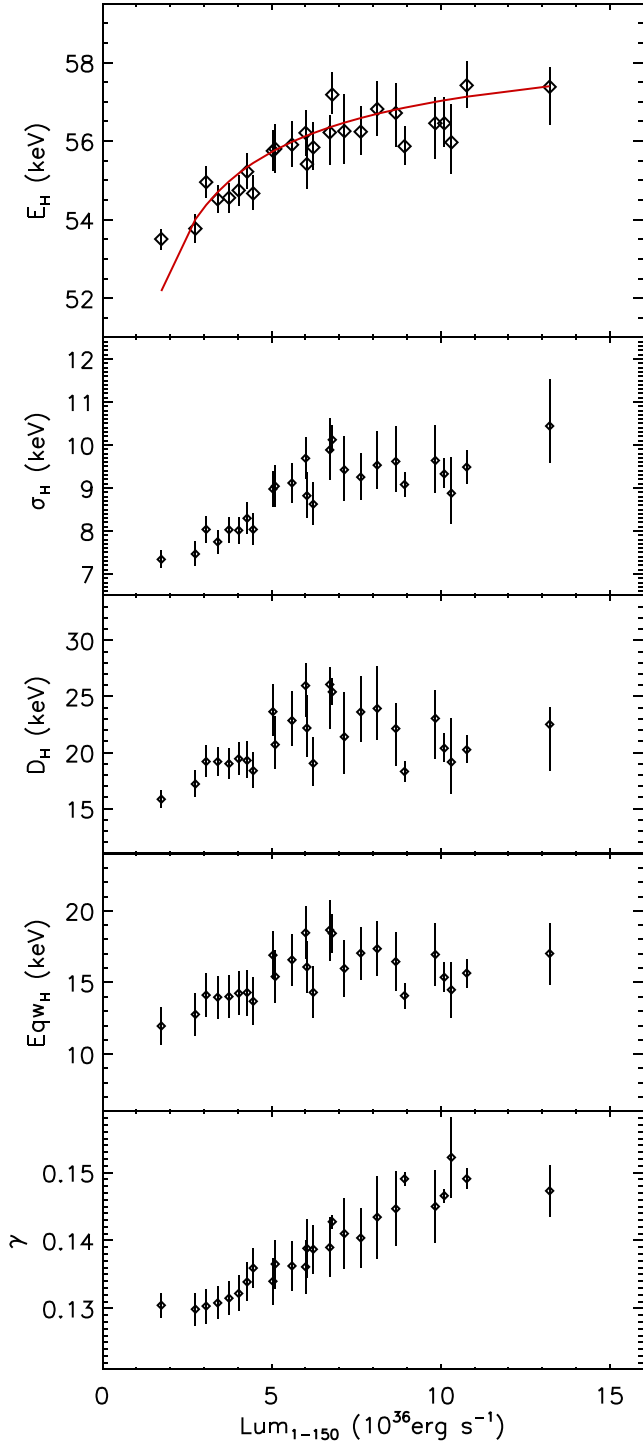


Figure 3. Best-fitting parameters versus source luminosity for the spectra extracted along the entire survey interval. From top to bottom: line energy, width, strength, equivalent width, Comptonization parameter. The solid line in the top panel is the theoretical prediction for $E_* = 29.56$ keV (see equation 2).

The energy of the second harmonic is directly correlated with the luminosity (with a correlation coefficient of 0.89, and a corresponding probability of no correlation of $\sim 1.0 \times 10^{-9}$), confirming the results reported by Fürst et al. (2014) from the analysis of two *NuSTAR* observations. This correlation, observed for the first time in Her X-1 (Staubert et al. 2007), is expected

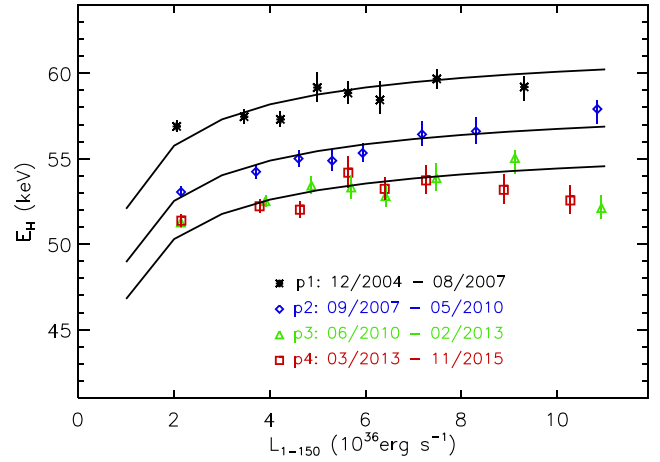


Figure 4. Energy of the second harmonic versus source luminosity for the four 33-month time intervals. The continuous lines in the figure are theoretical predictions (see equation 2) for $E_* = 28.25, 29.42, 31.12$ keV (bottom to top, respectively). The E_* values were obtained fitting each set of data with equation (2). Data sets p3 and p4 were fitted together.

in the subcritical accretion regime ($L_{\text{coul}} < L < L_{\text{crit}}$; see Becker et al. 2012), where the deceleration of the material to rest at the stellar surface is accomplished by a shock dominated by Coulomb interactions. The ram pressure of the infalling plasma increases with the accretion rate driving the shock region down to regions of higher magnetic field intensity. Using equations (51) and (58) in Becker et al. (2012), we can derive the energy/luminosity correlation for the fundamental CRSF:

$$E_F = \left[1 + 0.6 \left(\frac{R_*}{10 \text{ km}} \right)^{-\frac{13}{14}} \left(\frac{\Lambda}{0.1} \right)^{-1} \left(\frac{\tau_*}{20} \right) \left(\frac{M_*}{1.4 M_\odot} \right)^{\frac{10}{14}} \right. \\ \left. \times \left(\frac{E_*}{1 \text{ keV}} \right)^{-\frac{4}{7}} \left(\frac{L_x}{10^{37} \text{ erg s}^{-1}} \right)^{-\frac{5}{7}} \right]^{-3} \times E_*, \quad (2)$$

where τ_* is the Thomson optical depth (~ 20 for typical HMXB parameters; Becker et al. 2012), R_* is the radius of the NS, M_* is the mass of the NS, E_* is the energy of the fundamental cyclotron line at the NS surface and Λ is a constant related to the interaction between the magnetic field and the surrounding medium (Lamb, Pethick & Pines 1973). We adopt the values $\Lambda = 1$, suitable for spherical accretion, $R_* = 10$ km and $M_* = 1.8 M_\odot$ (Rawls et al. 2011) as in Fürst et al. (2014). The energy of the CRSF depends on the accretion rate in good agreement with theoretical predictions: a fit of the data using as best-fitting model equation (2) yields $E_* = 29.56 \pm 0.05$, with $\chi^2 = 1.8$, assuming a harmonic ratio of 2 (solid line in the top panel of Fig. 3).

Mushtukov et al. (2015) have proposed an alternative theory to explain the positive correlation between CRSF energy and luminosity in subcritical sources: the bulk of the radiation, emitted by the hotspot on the polar cap, travels upwards through the accretion channel interacting with the infalling matter and producing the CRSF at the resonant energies. The line appears redshifted by Doppler effect to the observer due to the velocity profile of the plasma falling towards the NS surface. The higher the luminosity, the lower is the velocity of plasma, slowed by the radiation pressure, and the smaller is the Doppler shift of the line. At the limit of the critical luminosity that marks the balance between radiation pressure and ram pressure of the matter, no Doppler shift is observed and the line energy corresponds to the value defined by

Table 2. Spectral fit results from the count-rate-selected spectra extracted along the four 33-month time intervals. The columns are described in Table 1.

Sp	E_H (keV)	σ_H (keV)	D_H	kT (keV)	τ	L_{36} (erg s $^{-1}$)	χ^2
p1-1	56.9 $^{+0.3}_{-0.3}$	7.9 $^{+0.3}_{-0.3}$	20.1 $^{+1.2}_{-1.1}$	9.0 $^{+0.1}_{-0.1}$	7.6 $^{+0.1}_{-0.1}$	2.05	1.66
p1-2	57.5 $^{+0.4}_{-0.4}$	8.3 $^{+0.3}_{-0.3}$	20.9 $^{+1.6}_{-1.4}$	8.5 $^{+0.1}_{-0.1}$	8.2 $^{+0.1}_{-0.1}$	3.46	1.42
p1-3	57.3 $^{+0.5}_{-0.4}$	8.1 $^{+0.4}_{-0.4}$	19.9 $^{+1.7}_{-1.5}$	8.1 $^{+0.1}_{-0.1}$	8.9 $^{+0.1}_{-0.1}$	4.22	1.30
p1-4	59.2 $^{+0.9}_{-0.8}$	9.4 $^{+0.7}_{-0.6}$	24 $^{+3}_{-3}$	8.0 $^{+0.2}_{-0.1}$	9.2 $^{+0.2}_{-0.2}$	4.99	1.21
p1-5	58.8 $^{+0.7}_{-0.6}$	9.0 $^{+0.6}_{-0.5}$	23 $^{+3}_{-2}$	7.8 $^{+0.1}_{-0.1}$	9.4 $^{+0.2}_{-0.2}$	5.63	1.19
p1-6	58.4 $^{+1.1}_{-0.8}$	9.6 $^{+0.8}_{-0.7}$	22 $^{+3}_{-3}$	7.6 $^{+0.1}_{-0.1}$	10.2 $^{+0.3}_{-0.2}$	6.29	1.80
p1-7	61.2 $^{+0.5}_{-0.8}$	11.1 $^{+0.5}_{-1.4}$	32.8 $^{+0.9}_{-8.2}$	7.6 $^{+0.1}_{-0.3}$	10.3 $^{+0.1}_{-0.1}$	7.73	1.66
p1-8	59.2 $^{+0.7}_{-0.8}$	9.7 $^{+0.9}_{-0.7}$	24 $^{+2}_{-3}$	7.2 $^{+0.1}_{-0.2}$	11.1 $^{+0.4}_{-0.3}$	9.31	1.48
p2-1	53.1 $^{+0.3}_{-0.3}$	6.7 $^{+0.3}_{-0.3}$	15.7 $^{+1.0}_{-1.0}$	8.3 $^{+0.1}_{-0.1}$	8.0 $^{+0.1}_{-0.1}$	2.14	1.19
p2-2	54.2 $^{+0.4}_{-0.4}$	7.5 $^{+0.3}_{-0.3}$	18.6 $^{+1.4}_{-1.3}$	8.1 $^{+0.1}_{-0.1}$	8.2 $^{+0.1}_{-0.1}$	3.71	1.71
p2-3	55.0 $^{+0.5}_{-0.5}$	8.4 $^{+0.4}_{-0.4}$	21.8 $^{+2.1}_{-1.9}$	8.0 $^{+0.1}_{-0.1}$	8.6 $^{+0.2}_{-0.2}$	4.60	0.77
p2-4	54.9 $^{+0.7}_{-0.6}$	8.3 $^{+0.5}_{-0.5}$	19 $^{+3}_{-2}$	7.6 $^{+0.2}_{-0.1}$	9.2 $^{+0.2}_{-0.2}$	5.30	0.92
p2-5	55.3 $^{+0.6}_{-0.5}$	8.4 $^{+0.5}_{-0.4}$	21 $^{+2}_{-2}$	7.5 $^{+0.1}_{-0.1}$	9.4 $^{+0.2}_{-0.2}$	5.93	0.96
p2-6	56.4 $^{+0.8}_{-0.7}$	9.4 $^{+0.6}_{-0.6}$	25 $^{+4}_{-3}$	7.6 $^{+0.2}_{-0.2}$	9.3 $^{+0.3}_{-0.3}$	7.17	1.00
p2-7	56.6 $^{+0.8}_{-0.7}$	9.0 $^{+0.7}_{-0.6}$	22 $^{+3}_{-3}$	7.2 $^{+0.2}_{-0.1}$	10.2 $^{+0.3}_{-0.3}$	8.30	0.72
p2-8	57.9 $^{+0.5}_{-0.8}$	10.3 $^{+0.9}_{-0.7}$	28 $^{+2}_{-4}$	7.3 $^{+0.1}_{-0.2}$	10.0 $^{+0.3}_{-0.2}$	10.83	1.12
p3-1	51.3 $^{+0.3}_{-0.3}$	6.7 $^{+0.3}_{-0.3}$	14.3 $^{+1.0}_{-0.9}$	8.2 $^{+0.1}_{-0.1}$	3.5 $^{+0.1}_{-0.1}$	2.14	1.53
p3-2	52.5 $^{+0.3}_{-0.3}$	7.2 $^{+0.3}_{-0.3}$	18.3 $^{+1.3}_{-1.2}$	8.0 $^{+0.1}_{-0.1}$	8.0 $^{+0.1}_{-0.1}$	3.91	1.11
p3-3	53.4 $^{+0.5}_{-0.5}$	8.1 $^{+0.4}_{-0.4}$	20.0 $^{+2.0}_{-1.9}$	7.7 $^{+0.1}_{-0.1}$	8.6 $^{+0.2}_{-0.2}$	4.87	0.67
p3-4	53.3 $^{+0.7}_{-0.7}$	8.4 $^{+0.5}_{-0.5}$	22 $^{+3}_{-3}$	7.6 $^{+0.2}_{-0.2}$	8.7 $^{+0.2}_{-0.2}$	5.70	1.27
p3-5	52.8 $^{+0.7}_{-0.6}$	8.0 $^{+0.6}_{-0.5}$	19 $^{+3}_{-2}$	7.3 $^{+0.2}_{-0.2}$	9.3 $^{+0.3}_{-0.3}$	6.41	1.40
p3-6	53.9 $^{+0.9}_{-0.8}$	9.2 $^{+0.7}_{-0.6}$	24 $^{+4}_{-3}$	7.3 $^{+0.2}_{-0.2}$	9.5 $^{+0.3}_{-0.3}$	7.47	0.77
p3-7	55.0 $^{+0.5}_{-0.9}$	10.0 $^{+0.8}_{-0.8}$	29 $^{+1}_{-5}$	7.3 $^{+0.1}_{-0.2}$	9.5 $^{+0.4}_{-0.2}$	9.11	1.22
p3-8	52.1 $^{+0.7}_{-0.7}$	7.4 $^{+0.7}_{-0.6}$	15 $^{+3}_{-2}$	6.4 $^{+0.1}_{-0.1}$	11.4 $^{+0.4}_{-0.4}$	10.92	1.23
p4-1	51.4 $^{+0.4}_{-0.3}$	6.9 $^{+0.3}_{-0.3}$	15.0 $^{+1.1}_{-1.0}$	8.2 $^{+0.1}_{-0.1}$	8.0 $^{+0.1}_{-0.1}$	2.15	1.53
p4-2	52.2 $^{+0.4}_{-0.4}$	7.6 $^{+0.3}_{-0.3}$	18.2 $^{+1.5}_{-1.4}$	7.9 $^{+0.1}_{-0.1}$	8.4 $^{+0.1}_{-0.1}$	3.78	1.08
p4-3	52.0 $^{+0.5}_{-0.5}$	7.1 $^{+0.4}_{-0.4}$	15.1 $^{+1.6}_{-1.4}$	7.3 $^{+0.1}_{-0.1}$	9.2 $^{+0.2}_{-0.2}$	4.62	0.57
p4-4	54.2 $^{+0.9}_{-0.9}$	9.3 $^{+0.7}_{-0.7}$	23 $^{+4}_{-4}$	7.7 $^{+0.2}_{-0.2}$	8.8 $^{+0.3}_{-0.3}$	5.63	1.18
p4-5	53.2 $^{+0.7}_{-0.6}$	8.7 $^{+0.5}_{-0.5}$	22 $^{+3}_{-3}$	7.5 $^{+0.2}_{-0.2}$	9.1 $^{+0.2}_{-0.2}$	6.39	1.22
p4-6	53.7 $^{+0.9}_{-0.8}$	8.6 $^{+0.7}_{-0.7}$	20 $^{+4}_{-3}$	7.1 $^{+0.2}_{-0.2}$	9.8 $^{+0.3}_{-0.3}$	7.26	0.94
p4-7	53.2 $^{+0.9}_{-0.8}$	8.7 $^{+0.8}_{-0.7}$	19 $^{+4}_{-3}$	6.9 $^{+0.2}_{-0.2}$	10.2 $^{+0.4}_{-0.4}$	8.88	0.97
p4-8	52.6 $^{+0.9}_{-0.8}$	7.6 $^{+0.8}_{-0.7}$	14 $^{+3}_{-2}$	6.5 $^{+0.2}_{-0.1}$	11.4 $^{+0.4}_{-0.4}$	10.27	1.38

the surface magnetic field. In this framework, the width of the line is also expected to correlate positively with the luminosity, since an increase of the radiation pressure produces a layer of infalling matter at lower velocity, extending bluewards the line profile. These trends are indeed observed in our results (Fig. 3).

We have investigated if this correlation evolves on a yearly time-scale, splitting the survey data into four 33-month intervals. We observe a significant shift in energy of this correlation along the time, except for the last two intervals, where the measurements overlap. The correlation coefficients for each data set are 0.83 (p -value = 0.010), 0.99 (p -value = 4.3×10^{-6}) and 0.47 (p -value = 0.066) for p1, p2 and p3+p4, respectively. The theoretical correlation matches the observed data for different values of the en-

ergy of the fundamental at the stellar surface (28.25 ± 0.07 , 29.42 ± 0.09 and 31.12 ± 0.10 keV, with χ^2 of 2.3, 1.2 and 2.4, respectively; solid lines in Fig. 4). This translates into a decrease of the fundamental line of ~ 0.36 keV yr $^{-1}$ along the first three time intervals, corresponding to a decay of the surface magnetic field intensity of $\sim 3 \times 10^{10}$ G yr $^{-1}$.

We have checked if this shift could be due to a systematic drift of the instrumental energy/channel gain. Such a drift would produce a significant variation in the slope of the Crab spectrum along the time. Therefore, we accumulated the Crab spectra in the four time intervals and fitted them with a power law. The variation of the Crab power-law photon index between the last and the first time intervals is $+0.017 \pm 0.006$. If this was due to a variation in the

channel/energy gain, this would correspond to an uncertainty in the energy determination of only ~ 0.2 keV, negligible with respect to the statistical uncertainty on the line position.

A long-term decay in the magnetic field, unrelated to the source luminosity, was recently assessed in the persistent accreting pulsar Her X-1 (Staubert et al. 2014, 2016), where the cyclotron line energy decreased on average by 0.26 keV yr^{-1} between 1996 and 2012. This long-term decay is most likely a local effect confined to the magnetic polar cap: it could be related to the accreted matter that accumulates into a magnetically supported mound and causes either a distortion of the magnetic field lines (Brown & Bildsten 1998) or a geometrical displacement of the emission region. The observed break in the decay after the third time interval could be explained if this mound has reached a maximum size for a stable structure (Litwin, Brown & Rosner 2001; Mukherjee & Bhattacharya 2012) and the plasma settling on it is balanced by the plasma leaking out from its base. A similar interpretation was adopted to explain the drop of the magnetic field in V0332+53 during the 2015 outburst, where a difference of ~ 1.5 keV in the CRSF fundamental line energy was observed between the start and the end of the outburst (Cusumano et al. 2016).

With an average luminosity of $\sim 3.0 \times 10^{36}$ erg s^{-1} Vela X-1 accretes at $\sim 0.36 \times 10^{-9} M_{\odot} \text{yr}^{-1}$, while the average luminosity of $\sim 10^{37}$ erg s^{-1} in Her X-1 corresponds to $\sim 10^{-9} M_{\odot} \text{yr}^{-1}$ (Klochkov et al. 2015). If the accreted matter is the cause of the decay of the magnetic field along the accretion column, this mechanism is a factor of ~ 4 more efficient in Vela X-1 than in Her X-1. This difference could be related to a narrower accretion column in Vela X-1, that, following equation (23) in Becker et al. (2012), is ~ 0.4 km with respect to ~ 1.3 km in Her X-1 and allows for a faster growth of the height of the mound. Indeed, the accreted mass per unit surface is $\sim 7.2 \times 10^{-10} M_{\odot} \text{km}^{-2} \text{yr}^{-1}$ in Vela X-1, a factor of ~ 4 higher than $\sim 1.9 \times 10^{-10} M_{\odot} \text{km}^{-2} \text{yr}^{-1}$ in Her X-1.

As shown in fig. 4 in Staubert et al. (2014), the CRSF energy in Her X-1 was constant before 1991. Between 1991 and 1995, a drop of ~ 8 keV was observed, followed by a more linear decay after 1995. One explanation might be a cyclic behaviour of the CRSF energy, and the jump could be induced by a destructive event that destroys the mound and resets the line emission region to the pre-mound configuration. Vela X-1 could have entered a stable configuration in the last time interval. An abrupt recovery of the line energy to a higher value in the next years could be therefore expected if the same restoring mechanism observed in Her X-1 works also in Vela X-1.

ACKNOWLEDGEMENTS

This work was supported by contract ASI I/004/11/0. We thank the anonymous referee for comments that helped improve the paper.

Facility: *Swift*

REFERENCES

- Barthelmy S. D. et al., 2005, *Space Sci. Rev.*, 120, 143
Becker P. A. et al., 2012, *A&A*, 544, A123

- Brown E. F., Bildsten L., 1998, *ApJ*, 496, 915
Choi C. S., Dotani T., Day C. S. R., Nagase F., 1996, *ApJ*, 471, 447
Cusumano G., La Parola V., D’Ài A., Segreto A., Tagliaferri G., Barthelmy S. D., Gehrels N., 2016, *MNRAS*, 460, L99
Fürst F. et al., 2010, *A&A*, 519, A37
Fürst F. et al., 2014, *ApJ*, 780, 133
Gehrels N. et al., 2004, *ApJ*, 611, 1005
Hiltner W. A., Werner J., Osmer P., 1972, *ApJ*, 175, L19
Kendziorra E. et al., 1992, in Tanaka Y., Koyama K., eds, *Proceedings of the Yamada Conference XXVIII. Frontiers Science Series. Universal Academy Press, Tokyo*, p. 51
Klochkov D., Staubert R., Santangelo A., Rothschild R. E., Ferrigno C., 2011, *A&A*, 532, A126
Klochkov D., Staubert R., Postnov K., Wilms J., Rothschild R. E., Santangelo A., 2015, *A&A*, 578, A88
Kretschmar P. et al., 1997, *A&A*, 325, 623
Kreykenbohm I., Coburn W., Wilms J., Kretschmar P., Staubert R., Heindl W. A., Rothschild R. E., 2002, *A&A*, 395, 129
Kreykenbohm I. et al., 2008, *A&A*, 492, 511
La Barbera A., Santangelo A., Orlandini M., Segreto A., 2003, *A&A*, 400, 993
Lamb F. K., Pethick C. J., Pines D., 1973, *ApJ*, 184, 271
Litwin C., Brown E. F., Rosner R., 2001, *ApJ*, 553, 788
McClintock J. E. et al., 1976, *ApJ*, 206, L99
Maitra C., Paul B., 2013, *ApJ*, 763, 79
Makishima K., Mihara T., 1992, in Tanaka Y., Koyama K., eds, *Proceedings of the Yamada Conference XXVIII. Frontiers Science Series. Universal Academy Press, Tokyo*, p. 23
Mukherjee D., Bhattacharya D., 2012, *MNRAS*, 420, 720
Mushtukov A. A., Tsygankov S. S., Serber A. V., Suleimanov V. F., Poutanen J., 2015, *MNRAS*, 454, 2714
Odaka H., Khangulyan D., Tanaka Y. T., Watanabe S., Takahashi T., Makishima K., 2013, *ApJ*, 767, 70
Orlandini M. et al., 1998, *A&A*, 332, 121
Rawls M. L., Orosz J. A., McClintock J. E., Torres M. A. P., Bailyn C. D., Buxton M. M., 2011, *ApJ*, 730, 25
Sadakane K., Hirata R., Jugaku J., Kondo Y., Matsuoka M., Tanaka Y., Hammerschlag-Hensberge G., 1985, *ApJ*, 288, 284
Schanne S., Götz D., Gérard L., Sizun P., Falanga M., Hamadache C., Cordier B., von Kienlin A., 2007, in Grebenev S., Sunyaev R., Winkler C., eds, *ESA SP-622: The Obscured Universe. ESA, Noordwijk*, p. 479
Schönherr G., Wilms J., Kretschmar P., Kreykenbohm I., Santangelo A., Rothschild R. E., Coburn W., Staubert R., 2007, *A&A*, 472, 353
Segreto A., Cusumano G., Ferrigno C., La Parola V., Mangano V., Mineo T., Romano P., 2010, *A&A*, 510, A47
Staubert R., Shakura N. I., Postnov K., Wilms J., Rothschild R. E., Coburn W., Rodina L., Klochkov D., 2007, *A&A*, 465, L25
Staubert R., Klochkov D., Wilms J., Postnov K., Shakura N. I., Rothschild R. E., Fürst F., Harrison F. A., 2014, *A&A*, 572, A119
Staubert R., Klochkov D., Vybornov V., Wilms J., Harrison F. A., 2016, *A&A*, 590, 91
van Kerkwijk M. H., van Paradijs J., Zuiderwijk E. J., Hammerschlag-Hensberge G., Kaper L., Sterken C., 1995, *A&A*, 303, 483

This paper has been typeset from a $\text{\TeX}/\text{\LaTeX}$ file prepared by the author.